LANGMUIR Article
Cite This: Langmuir 2019, 35, 5324−5332 pubs.acs.org/Langmuir

Atomistic Study of Dynamic Contact Angles in CO_2−Water−Silica System

Pengyu Huang,[†] Luming Shen,*[,†] Yixiang Gan,[†] Federico Maggi,[†] Abbas El-Zein,[†] and Zhejun Pan[‡]

[†]School of Civil Engineering, Building J05, The University of Sydney, Sydney, NSW 2006, Australia
[‡]CSIRO Energy, Private Bag 10, Clayton South, VIC 3169, Australia

Supporting Information

ABSTRACT: The dynamic wetting for the CO_2−water−silica system occurring in deep reservoirs is complex because of the interactions among multiple phases. This work aims to quantify the contact angle of CO_2−water flow in the silica channel at six different flow velocities using molecular dynamics. The dynamic contact angle values at different contact line velocities are obtained for the CO_2−water−silica system. By calculating the rates of the adsorption−desorption process of CO_2 and water molecules on the silica surface using molecular dynamics simulations, it has been found that the results of the dynamic contact angle can be explained by the molecular kinetic theory and predicted from the equilibrium molecular simulations. Moreover, the capillary pressure at different contact line velocities is predicted according to the Young−Laplace equation. The change in contact angles at different velocities is compared with empirical equations in terms of capillary number. The results of this study can help us better understand the dynamic process of the multiphase flow at the nanoscale under realistic reservoir conditions.

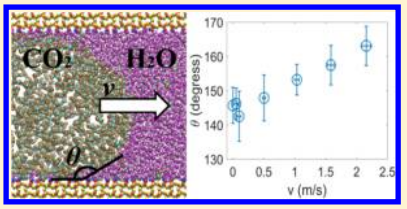

INTRODUCTION

The study of multiphase flow in porous media, such as supercritical CO_2−water flow in sedimentary aquifers, is crucial in geoscience, petroleum engineering, and environmental engineering. For example, evaluation of the viability CO_2 geosequestration in saline aquifers requires an understanding of the multiphase interactions between supercritical CO_2, water (or brines), and the rocks in reservoirs and caprocks. There are four major trapping mechanisms in CO_2 geosequestration in saline aquifers: structural trapping, residual trapping, solubility trapping, and mineral trapping.[1] The first two trapping mechanisms depend on the capillary forces and wettability in the caprock and reservoir.[2−4] The capillary pressures in small pores, especially nano-sized pores, which are common in caprock, can be relatively large and play an important role in the flow of fluids in micro- and nanoporous media.

Wettability is usually quantified as a contact angle in a fluid−fluid−solid system or a gas−fluid−solid system. Since the injection of CO_2 in geosequestration is a dynamic process,[5] we focus on the study of static and dynamic contact angles of a CO_2−water−silica system in this work. The static contact angle is obtained when the three-phase contact line does not move relative to the solid surface; the dynamic contact angle is obtained when the contact line moves at a certain velocity relative to the solid surface. The silica surface is considered because quartz is one of the common constituents in reservoirs and the caprocks.[5] The static contact angle in CO_2−water (or brine)−silica systems has been studied intensively in experiments[2−4] and molecular dynamics (MD) simulations at different environmental conditions, such as different pressures, temperatures, brine concentrations, and hydroxyl functional groups on the silica surfaces.[6−9] There were some ambiguities on the effect of CO_2 pressure on the experimentally measured water contact angle (a contact angle measured from the water phase) due to surface contaminations and chemical reactions, which have been discussed in the literature.[6,10] The MD simulations provide a reasonably consistent trend for the dependence of contact angles on pressure: the water contact angle increases significantly with increasing pressure when approaching the CO_2 critical pressure.[6−8] Iglauer et al. attributed such increase to the large increase in the density of CO_2 until the saturation pressure of CO_2 is reached.[7] In addition to CO_2−water−silica systems, contact angles for CO_2−brine−kaolinite systems with both hydrophobic and hydrophilic surfaces have also been calculated using MD by Tenney and Cygan.[11] As for dynamic contact angles, a few experiments studying supercritical CO_2−water displacement have been reported in the literature.[12,13] To our knowledge, there has been no investigation of the effect of flow rates on dynamic contact angles for the CO_2−water−silica system at the nanoscale. The behavior of the contact angle at different contact line velocities can directly affect the calculation of the capillary pressure based on the Young−Laplace equation. For example, the modified Lucas−Washburn equation used in predicting the behavior of capillary flow, which considers the dynamic contact angle, provides better estimations than the original Lucas−Washburn equation with the assumption of a static contact angle,[14] but it excludes the effects of all phases. More recently, the inclusion of multiple phases and phases

Received: January 8, 2019
Revised: March 10, 2019
Published: March 14, 2019

DOI: 10.1021/acs.langmuir.9b00076
Langmuir 2019, 35, 5324−5332

with multiple miscible components in the Lukas−Washburn equation highlight non-negligible effects of the phases on the contact angle.[15,16]

For the capillary flow in the nanochannels, it has been found that the filling rate is slower than the one calculated from the Lukas−Washburn equation, which showed a deviation from the results at the macroscopic scale.[17−19] The slower capillary filling rate has been attributed to the viscous resistance of the air phase by Hultmark et al.,[19] whereas Chauvet et al. considered the effect of gas pressurization on the imbibition rates, by taking account of the compressibility of the gas.[17] Oyarzua et al. found that an increase in air pressure can slow down the imbibition rate, and the air pressure can be accumulated at the capillary front by modeling the spontaneous imbibition of water in slit silica using MD simulations. Hence, they suggested that the pressurization of the air can be important in the capillary filling process at the nanoscale.[18] There have been studies showing that the dynamic contact angle at the nanoscale plays an important role in capillary filling using MD simulations as well.[20,21] These studies show the importance of investigating multiphase flow and the dynamic contact angle at the nanoscale.

Both experiments[22−25] and MD simulations of simple fluids (Lennard-Jones fluid particles)[21,26−28] show the dynamic contact angle θ_d changes with the contact line velocity v. Two theories are commonly used to describe dynamic wetting: a hydrodynamic theory[29] and a molecular kinetic theory[30] (MKT). The hydrodynamic theory suggests that the viscous bending of the liquid−gas interface is the main cause of changes in the macroscopic dynamic contact angle, whereas the microscopic angle is usually assumed to be kept at its static contact angle θ_s.[29] MKT relates the movement of the three-phase contact line zone to the adsorption and desorption process of the liquid molecules on the solid surfaces. There are two key parameters in MKT: the equilibrium jump frequency K_o and the average jump distance λ of one molecule from one adsorption site to another. Although these two parameters having seemingly physical meanings are usually obtained by fitting experimental or simulation data to the MKT equation, they can also be estimated from the statistical analysis of MD simulations, which has been validated from MD simulations of the Lennard-Jones chain beads.[31,32] However, it has not been validated with realistic molecular models such as those simulating water molecules. Apart from theoretical models, researchers have also derived an empirical power-law correlation expressing the dynamic contact angle as a function of the dimensionless capillary number C_a for the liquid−vapor−solid system, with $C_a = \mu v/\gamma$, where μ is the dynamic viscosity of the liquid phase, v is the contact line velocity, and γ is the interfacial tension between the two fluids.[22−25]

The objective of this study is to investigate the effect of contact line velocity on the dynamic contact angles for the CO_2−water−silica system using MD simulations and gain fundamental understandings of dynamic wetting at the nanoscale. In this work, the static contact angles at different pressures will be simulated and validated against the available experimental and numerical data.[3,6,33,34] Dynamic contact angles at different flow velocities under high pressure and temperature conditions will then be studied using MD simulations. In the literature, the dynamic contact angle has been measured under changing contact line velocities, such as the capillary rise[15] and droplet spreading,[35] and under constant velocities, such as Couette flow[36] and curtain coating.[37] It has been shown that the dynamic contact angle is related to not only the velocity but also the acceleration of the contact line.[38] In this work, the dynamic contact angle will be studied under a constant flow velocity and the effect of acceleration of the contact line is not investigated. The simulated dynamic contact angle results will be explained within the framework of MKT, with jump frequency K_o and distance λ extracted at the nanoscale. After defining the λ values in parallel and perpendicular directions relative to the solid surfaces ($\lambda_\parallel$ and $\lambda_\perp$), the parallel and perpendicular jump frequency $K_{o,\parallel}$ and $K_{o,\perp}$ will be calculated through the statistical analysis of the motions of molecules. The fitted $K_{o,\parallel}$ and $K_{o,\perp}$ values will also be obtained by fitting the MKT equation to the dynamic contact angle results from MD simulations, given $\lambda_\parallel$ and $\lambda_\perp$, and the area density of the adsorption site. The calculated $K_{o,\parallel}$ and $K_{o,\perp}$ values from the molecular motions will be compared with the fitted $K_{o,\parallel}$ and $K_{o,\perp}$ values for the validation of the MKT for realistic molecular systems. The estimated capillary pressure as a function of the contact line velocity will also be shown. Finally, our simulation results will be compared with the existing empirical equations for the dynamic contact angle as a power-law function of the capillary number. A new understanding of nanoscale dynamic wetting behavior such as dependence of capillary pressure on contact line velocity will be beneficial to the development of future physics-based, pore-scale multiphase flow models, which will, in turn, enhance the accuracy of reservoir modeling.

COMPUTATIONAL METHOD

The CO_2−water−silica systems are modeled to calculate the static and dynamic contact angles. The TIP4P/2005 water model and the flexible EMP2 CO_2 model[39] are adopted for the modeling of liquids. The TIP4P/2005 water model can accurately reproduce experimental values of surface tension and performs best among available water models.[40] The EMP2 model has also been commonly used to model CO_2 in MD simulations and, along with the TIP4P/2005 model, to study interfacial tension and static contact angles at different pressures and temperatures.[7] The silica surface is modeled using the force fields recently developed by Emami et al., and the structures of the surface model can be obtained from their database.[41] In particular, the surface model with the Q^3 surface environment is used (see Figure S1 in the Supporting Information), which provides a similar (Si−O−H) density as the average area density of the amorphous silica in aqueous environments.[42]

All simulations are carried out using the LAMMPS code.[43] The VMD has been used to visualize and to generate figures in this study.[44] The VMD[44] and the TopoTools[45] (VMD plugin) have been used to construct silica slabs and a piston in the system. We construct two silica slabs and place CO_2 and water molecules between the two slabs in our simulations. A piston, which is made of silica, has been placed at the left end of the simulation box (see Figure 1a). The simulation box has a dimension of 33.37 nm × 3.484 nm × 12 nm. The channel height is 6.57 nm, which is calculated as the averaged distance between the oxygen atoms on the two silica internal surfaces. The area density of silanol groups on the silica surface is calculated as 4.8 nm^{-2} by dividing the total number of silanol groups on the surface by the surface area in the x−y plane. Periodic boundary conditions are applied in the x- and y-directions, whereas nonperiodic boundary conditions are applied in the z-direction. The atoms in the outer layers of

DOI: 10.1021/acs.langmuir.9b00076
Langmuir 2019, 35, 5324−5332

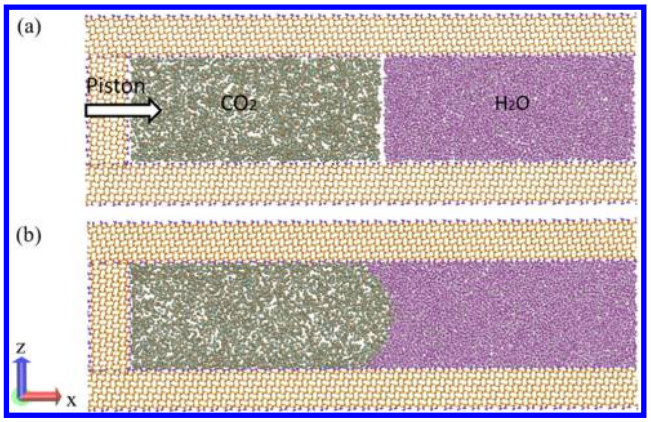

Figure 1. (a) Snapshot of the initial setup for the contact angle simulation with 3379 CO_2 molecules and (b) a snapshot of the static contact angle simulation at the equilibrium state with 3379 CO_2 molecules. The snapshots are plotted using the visualization tool for molecular dynamics VMD.[44]

the top and bottom surfaces (about a third of the thickness of the silica slab) are fixed. A total of 11 310 water molecules is used, whereas six different numbers of CO_2 molecules are used to achieve different CO_2 pressures: 3672, 3379, 2820, 2359, 1352, and 459 molecules. The piston does not move in the simulations of the static contact angle. For the simulations of the dynamic contact angle, different velocities v_p = 0.05, 0.1, 0.5, 1, 1.5, and 2 m/s are applied to the piston for the simulation case with 3379 CO_2 molecules, since this simulation case leads to an equilibrium CO_2 pressure of 20.6 MPa and water pressure of 10.6 MPa (calculated from the static contact angle simulation), which fall within the range of real reservoir conditions. The effect of channel height on the contact angle, due to the line tension effect of the three-phase contact line,[46] is expected to be small in our MD simulation, because the periodicity in the *y*-axis in our system allows a zero curvature of the three-phase contact line and the size of our system is reasonably large. However, since the boundary effect for the interface interactions can be important at the nanoscale, it is still worth investigating the effect of channel height on the static and dynamic contact angle in the future.

The harmonic bond and harmonic angle functions are used for the intramolecular interactions except for the water molecules. The SHAKE algorithm[47] with a tolerance of 0.0001 is applied to constrain the bond length and angle of water molecules for allowing a longer time step. The Lennard-Jones potential and Coulombic interactions are used to describe the intermolecular interactions. The relevant equations and parameters for the molecular interactions are reported in Section S2 in the Supporting Information. A cut-off radius of 1.2 nm is chosen for the intermolecular interactions. The particle−particle particle−mesh (PPPM) method[48] with a relative error in forces of 10^{-5} and a slab correction (with a volume factor of 3 in LAMMPS)[49] is used to calculate long-range Coulombic interactions. This cut-off radius has been used in the simulations of inhomogeneous systems with the selected silica surface model.[41] Interactions between the piston and the silica slabs are excluded from the simulations. The charges on the atoms of the piston are set to zero to avoid the long-range Coulombic interactions between the piston and silica surfaces computed by the PPPM method. A time step of 1 fs (10^{-15} s) is used for all the simulations presented in this study. A water droplet with vacuum on the silica surface has been simulated (see Section S3 in the Supporting Information). A zero-contact angle is observed, which is the same as the contact angle result of Emami et al. for the Q^3 surface, although a flexible SPC water model was used in their simulation.[41] It has also been shown experimentally in the literature that the water on the fully hydroxylated quartz surface would result in a zero-contact angle.[50]

For the static case, each simulation is run for more than 10 ns at the NVT ensemble (isothermal ensemble) at 333.15 K. Since the supercritical CO_2 injection usually takes place at the deep reservoirs, a relatively high temperature compared to the temperature at the sea-level is used. The Langevin thermostat algorithm[51] is used to reach the thermal equilibrium quickly for the system during the first 1 ns and then a Nosé−Hoover chain thermostat[52] is applied for the rest of the simulation. Both Langevin and Nosé−Hoover chain thermostats are performed using the same damping parameter of 100 fs. The thermostat is applied to CO_2 and water molecules, and the free silica atoms in the inner layer of the silica slabs. The contact angle is obtained by plotting the interface from the two-dimensional

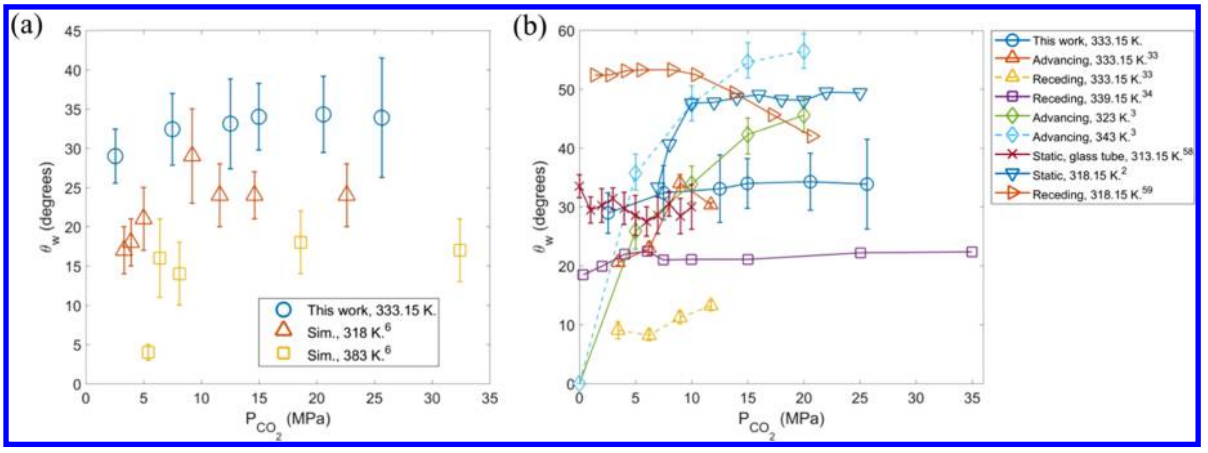

Figure 2. (a) Resulting static water contact angle against the CO_2 pressure in comparison with simulation results from ref 6; (b) the resulting water contact angle against the pressure in comparison with experimental results from the literature.[2,3,33,34,58,59] It is noted that the data from ref 59 is the first cycle measurement of the quartz surface because the quartz surface has been reused in ref 59. The data from refs 2 3 34 58 and 59 are obtained from their figures using an online tool WebPlotDigitizer.[60]

DOI: 10.1021/acs.langmuir.9b00076
Langmuir 2019, 35, 5324−5332

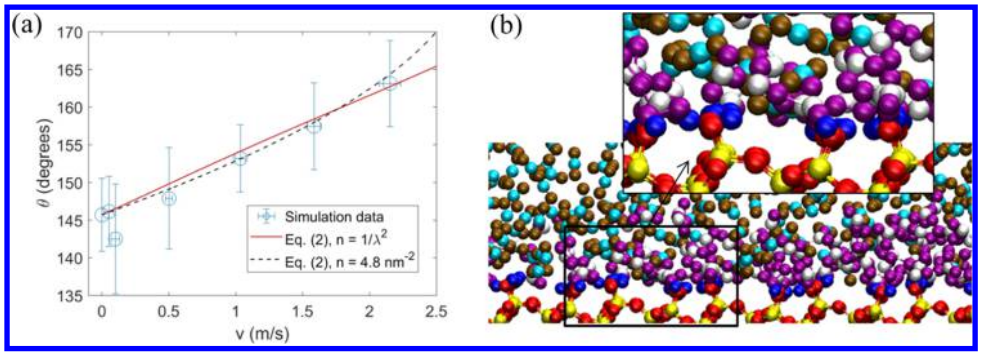

Figure 3. (a) CO_2 contact angle θ against the averaged contact line velocity v, under constant piston velocities (including zero velocity). Error bars are estimated from the standard deviations of the simulation data for each case. (b) Snapshot of the simulation with the piston velocity v_p = 1 m/s. CO_2 molecules are in cyan and ocher colors; the water molecules are in white and purple colors; the H and O atoms in the silanol groups are in blue and red, respectively. The inset in (b) is a zoom-in view of the surface and is plotted using the visualization tool VMD.[44]

water density profile at every 1 ns (see detailed calculations in Section S4 in the Supporting Information). Since the time-averaged interface profile does not change noticeably after 4 ns, the first 5 ns of the simulation are considered as the equilibrium run and the rest are considered as the production run. The pressures in CO_2 and water phases are obtained from the time-averaged pressures in bulk regions, which are away from the interfaces.

The initial configuration for the dynamic contact angle simulation is obtained from the end of the equilibrium run of the static contact angle simulation with 3379 CO_2 molecules. At first, the piston velocity increases linearly from 0 to the desired velocity for 0.2 ns to avoid the potential shock wave caused by the sudden increase of piston velocity. Then, each simulation for the dynamic case is run for 19 ns. For all cases except for v_p = 2 m/s, the contact angle and the contact line velocity are obtained at every 1 ns after the first 5 ns for average. Since it takes longer time for contact angle to reach equilibrium for the case of v_p = 2 m/s, the contact angle and the velocity are obtained at every 1 ns after 10 ns of the simulation. The contact line velocity is calculated from the time derivative of the average CO_2–water interface displacement.

RESULTS AND DISCUSSION

Static Contact Angle. Figure 1b shows a snapshot of the static contact angle simulation with 3379 CO_2 molecules at an equilibrium state. A curved interface has evolved because of the capillary pressure induced by the interfacial tension. The static water contact angles θ_w at different CO_2 pressures P_{Co_2} are plotted and compared with the simulations done by Chen et al.[6] in Figure 2a. It can be seen from Figure 2a that our simulated θ_w against pressure relation follows the similar trend obtained in the work of Chen et al.[6] Our simulations and the results of Chen et al. show an increase in the contact angle as pressure increases for P_{Co_2} < ∼10 MPa, although the increase in our contact angles from P = ∼3 to ∼7.5 MPa (3.4°) is less significant than that reported in Chen et al. The discrepancy in the contact angles can be caused by the different interfacial tensions between water and CO_2, and between water and silica, since Chen et al. used a flexible SPC/E water model in the simulation.[6] In addition, the contact angle was measured by modeling a cylindrical droplet in the work of Chen et al.,[6] which could result in a different contact angle value from that measured using the CO_2–water system between two plates in our simulations. For the system in thermodynamic equilibrium, the interfacial tensions should be balanced by Young's equation[53]

$$\gamma \cos\theta = \gamma_{sc} - \gamma_{sw} \quad (1)$$

where γ, γ_{sc}, and γ_{sw} represent the interfacial tensions between CO_2 and water, between silica and CO_2, and between silica and water, respectively. Therefore, the wettability alternation due to the change of pressure and CO_2 phase change depends on the changes in interfacial tensions. It should be noted that the validity of Young's equation at the nanoscale may still be debatable, but its validity at the nanoscale has recently been supported by studies using MD[54,55] and Monte Carlo simulations.[56] It is known that γ decreases rapidly with pressure for P < ∼10 MPa, and remains approximately constant for P > ∼10 MPa in both experiments and our CO_2–water interface simulations (see Section S6 in the Supporting Information for more details). Hence, in theory, the increase of the contact angle in the low-pressure range is due to the decrease of γ_{sc} and the increase of γ_{sw} with increasing pressure. Dickson et al.[57] proposed that the capping of the silanol groups on the quartz surface by the physical adsorption of the CO_2 molecules increases γ_{sw}, along with the decrease of γ_{sc} with increasing pressure, which results in an increase of the contact angle. Iglauer et al. also concluded based on their MD simulations that the wettability alternation with the increase of the pressure can be attributed to the rapid density changes in CO_2 and the strong CO_2–silica interactions.[7]

The simulation results are compared with the values of θ_w measured experimentally at various temperatures, as shown in Figure 2b. In particular, the experimental data were obtained from refs 3 33 and 34 at a temperature close to 333.15 K. The advancing and receding water contact angles have been extracted from the experimental data. It can be seen that there is a difference between the advancing and receding water contact angles from the experiments of Saraji et al.,[33] which is known as the contact angle hysteresis. Moreover, the different trends of the pressure-dependent contact angles have been observed experimentally. The contact angle can increase with pressure,[3,33] increase in the CO_2 phase transition range,[2,34] be independent of pressure,[58] or even decrease with the pressure.[59] These differences in the experimental data could be caused by surface contaminations and experimental techniques.[10] In addition, we use the Q^3 surface model in our simulations, whereas the area density of the hydroxyl groups in the experiments is unknown. Chen et al. also studied

DOI: 10.1021/acs.langmuir.9b00076
Langmuir 2019, 35, 5324–5332

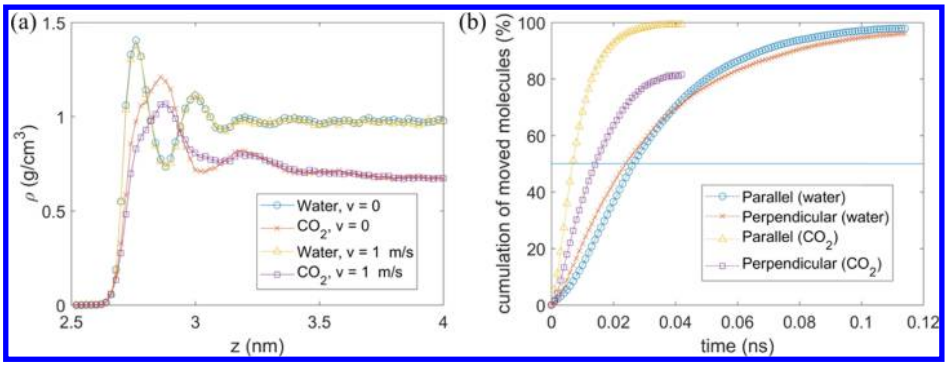

Figure 4. (a) Density profile along the z-axis (perpendicular to the solid surface) for both water and CO_2; (b) the average cumulative curve, which counts the number of molecules in the first layer (in percentage) that have moved a distance greater than the parallel jump distance $\lambda_{\parallel}$ and the perpendicular jump distance $\lambda_{\perp}$ for both water and CO_2, as a function of time. The horizontal solid line indicates the 50% mark, at which half the molecules in the first layer have moved a distance greater than $\lambda_{\parallel}$ or $\lambda_{\perp}$.

the contact angle against P for different silica surface models using MD (Q^2, Q^3, and amorphous Q^3 models, see ref 6 for details), and the observed different pressure dependencies of contact angles similar to many experimental studies: (1) the contact angle increases with pressure (Q^2 surface); (2) the contact angle first increases with pressure at low pressure (Q^3/amorphous Q^3 surface), and then shows no significant pressure dependence at high pressure. Our simulation results give a similar trend as Chen et al.'s results for the Q^3 surface model.[6] In the real world, the silica surface may consist of a combination of the various area densities of the silanol group and their protonated or deprotonated forms, which could be the reason that different contact angles and various pressure dependence were observed in the experiments.[6,9] Therefore, the purpose of the comparison of the simulated contact angles with the experiments is to confirm that the simulated contact angle values generally fall within the range of the experimental data.

Dynamic Contact Angle. CO_2 contact angles versus contact line velocity v are plotted in Figure 3a, obtained from the simulations of constant piston velocities (including zero velocity). It should be noted that here the CO_2 contact angles θ are used instead of water contact angles θ_w, i.e., $\theta = 180 - \theta_w$, since the CO_2 is the advancing/injecting fluid. It can be seen that θ increases when v increases for the studied CO_2–water–silica system. To gain a better understanding of the causes of the dynamic contact angle in multiphase flows from the molecular point of view, we analyze our results within the MKT framework.[30,61] The MKT describes the relationship between the dissipation processes of the liquid molecules at the three-phase contact line region, i.e., changes in the contact angles and the movement of the contact line. The Eyring's theory of absolute reaction rates[16,62] has been used in the derivation of the MKT to relate the equilibrium frequency of the thermal motions of the liquid molecules on the solid surface to the molar activation free energy,[30] which suggests that the MKT is a suitable thermodynamic model for describing the thermal motions of the liquid molecules on the solid surface at the contact line. At the equilibrium state (static contact angle case), the molecules within the contact line region can jump backward and forward from one adsorption site to another over an average jump distance λ at a jump frequency K_o. Hence, λ usually depends on the solid surface structures, which dominate the potential energy distribution, and K_o is related to the activation free energy of wetting. The unbalanced interfacial tension force $F = \gamma(\cos\theta_s - \cos\theta_d)$, due to any form of external forces, is the driving force causing the contact line to move along the solid surfaces by breaking the local equilibrium at the three-phase contact line, where θ_s and θ_d are the static and dynamic contact angles, respectively. The contact line velocity v can be expressed as a function of the change in the cosine of contact angle $\cos\theta_s - \cos\theta_d$[30,61]

$$v = 2K_o\lambda \sinh\left(\frac{\gamma(\cos\theta_s - \cos\theta_d)}{2nk_bT}\right) \quad (2)$$

where k_b is the Boltzmann's constant, T is the temperature in Kelvin, and n is the area density of the adsorption sites on the solid surface. For adsorption sites that are uniformly distributed on solid surfaces, one usually assumes that $n = 1/\lambda^2$, so that only two parameters (K_o and λ) in eq 2 need to be fitted against the calculated θ_s, θ_d, and v. As shown in Figure 3a, the solid line is fitted using eq 2, with the assumption $n = 1/\lambda^2$, resulting in the fitted parameters $K_o = 0.394$ GHz and $\lambda = 1.62$ nm. The value of λ should theoretically be in the same order of molecular size for the liquid–gas-solid system.[63] However, the fitted value of λ is 4–5 times larger than the molecular size (0.3–0.4 nm). The problem has been seen in the previous calculation of the fitting parameters in experimental studies of the liquid–liquid–solid system.[64] These discrepancies suggest that it could be inaccurate to determine the two parameters using eq 2 for the nanoscale system studied here through pure fitting processes.

The jump distances can be estimated from the MD simulations directly. Figure 3b shows a snapshot at the silica surface from the simulation with the piston velocity $v_p = 1$ m/s. In Figure 3b, the water molecules are adsorbed onto the silanol groups due to the strong hydrogen bonds, whereas the CO_2 molecules tend to fill the gaps between the adsorption sites. As a result, the liquid molecules form a crystalline-like layer structure near the solid surface.[65] The molecular jump can occur in the directions both perpendicular and parallel to the flow for the water and CO_2 molecules at the three-phase contact zone at the first layer. The jump distance in the parallel direction is assumed to be the distance between the two adjacent adsorption sites. We assume that the silanol groups are the adsorption site on the solid surfaces for water molecules. Since the area density of silanol groups is known as $n = 4.8$ nm^{-2} in our simulation, the λ value along the surface is then estimated as the parallel jump distance $\lambda_{\parallel} = (1/n)^{1/2} = 0.456$ nm. It should be noted that the jump distance in the x

DOI: 10.1021/acs.langmuir.9b00076
Langmuir 2019, 35, 5324–5332

Table 1. Calculated Parallel and Perpendicular Frequencies for Both Water and CO_2 Obtained from the Analysis of Static Contact Angle MD Simulation, and by Fitting eq 2 with the given Molecule Jump Distances

		$\lambda_{\parallel}$ (nm)	$K_{o,\parallel}$ (GHz)	$\lambda_{\perp}$ (nm)	$K_{o,\perp}$ (GHz)
MD	water	0.456	18.9 (±0.55)	0.24 (±0.013)	41.8 (±0.89)
	CO_2	0.456	73 (±1.03)	0.36 (±0.033)	70.6 (±0.93)
Equation 2	water/CO_2	0.456[a]	21.7	0.24[a]	41.3

[a] $\lambda_{\parallel}$ and $\lambda_{\perp}$ here are the input parameters to calculate $K_{o,\parallel}$ and $K_{o,\perp}$ by fitting eq 2.

and y-directions may not be the same for the given silica surface. Here, the $\lambda_{\parallel}$ = 0.456 nm is used for simplicity. In the direction perpendicular to the solid surface, the liquid density profile experiences large fluctuations and has layering structures due to the molecular interactions between the liquid and solid. Therefore, both water and CO_2 density profiles have two layers on top of the solid interface (Figure 4a). The density profiles are obtained from the equilibrium simulations by averaging the coordinate data obtained at every 0.1 ps over 1 ns. The distance between the first and second peaks of the density profile is considered as the perpendicular jump distance of a water molecule from the first layer to the second layer, i.e., $\lambda_{\perp}$ (water) = 0.24 nm. Similarly, perpendicular jump distance of a CO_2 molecule $\lambda_{\perp}$ (CO_2) = 0.36 nm is found. The block average method is used to estimate the error for $\lambda_{\perp}$.[66] The total 1000 samples of the instantaneous density profiles are divided into 10 blocks of 100 samples. An averaged density profile is calculated at each block, and hence $\lambda_{\perp}$ can be calculated as the block averaged value. The error of $\lambda_{\perp}$ can be estimated as the standard deviation of the 10 block values of $\lambda_{\perp}$. The density profiles at v_p = 1 m/s are also plotted in Figure 4a, obtained by averaging the coordinate data obtained at every 0.1 ps over 1 ns, after 5 ns. There is no significant change in the water density profile. The CO_2 density in the first layer in the dynamic case is smaller than the one in the static case along the z-direction, whereas the positions of the peak values are almost the same (see Figure 4a). The decrease in the CO_2 density in the first layer may be due to the small number of water molecules attached to the silanol groups, even the CO_2 has displaced the water. Hence, it is acceptable to use $\lambda_{\perp}$ (water) = 0.24 nm and $\lambda_{\perp}$ (CO_2) = 0.36 nm obtained from MD simulation of the static CO_2–water–silica system.

Having determined $\lambda_{\parallel}$ and $\lambda_{\perp}$ as described previously, the lateral and perpendicular frequencies, $K_{o,\parallel}$ and $K_{o,\perp}$, can be calculated separately, from the motions of CO_2 and water molecules in the first layer, based on the static contact angle simulations. These calculations are similar to that in the work of Ruijter et al.[31] Figure 4b shows the change in time of average cumulative percentages of water and CO_2 molecules which have moved a distance of $\lambda_{\perp}$ along the positive z-direction and $\lambda_{\parallel}$ in the x- or y-direction, away from their initial positions in the first layer. The detailed calculations of the average cumulative percentage curves are reported in Section S5 in the Supporting Information. Ma et al.[65] have shown that the time required for the water molecules on a carbon nanotube wall leaving the first layer at temperatures above 298 K is around 70 ps. It takes around 120 ps for the water molecules to leave the first layer on the silica surface in our simulation, which is broadly consistent with the calculations of Ma et al.[65] The average frequency is calculated as the inverse of the time needed for 50% of the molecules in the first layer to move a jump distance.[31] For the calculation of $K_{o,\parallel}$, the results should be divided by 2 because both the backward and forward motions are counted, as suggested by Bertrand et al.[32] Calculations of $K_{o,\perp}$ and $K_{o,\parallel}$ are reported in Table 1. Both values of $K_{o,\perp}$ and $K_{o,\parallel}$ obtained from water molecules are smaller than those of CO_2 molecules, although jump distances of water molecules are the same (in parallel direction) or smaller (in a perpendicular direction) than the jump distances of CO_2 molecules. Hence, it appears that the water molecules contribute more resistance to the breakage of the local equilibrium of the adsorption–desorption process when the contact line is moving.

On the other hand, $K_{o,\perp}$ and $K_{o,\parallel}$ can also be fitted using eq 2, given $\lambda_{\perp}$ and $\lambda_{\parallel}$ and n = 4.8 nm^{-2}. As n is given, only the term $2K_o\lambda$ in eq 2 is left to be determined by fitting the curve to the data. Results are reported in Table 1 and the fitted curve is also plotted in Figure 3a. $K_{o,\parallel}$ = 21.7 GHz is calculated with $\lambda_{\parallel}$ = 0.456 nm. Since water molecules provide more resistance than CO_2 molecules, we have used $\lambda_{\perp}$ (water) = 0.24 nm here to calculate $K_{o,\perp}$ for comparison purposes, which leads to $K_{o,\perp}$ = 41.3 GHz. Both $K_{o,\parallel}$ and $K_{o,\perp}$ obtained from eq 2 are similar to the values obtained from the MD simulations. These results suggest that the MKT works well for the CO_2–water–silica system under high pressure and temperature conditions if the value of λ is properly determined from MD simulations. It should be noted that the K_o values are calculated directly from the motions of molecules away from the CO_2–water interface, whereas the molecular behaviors at the three-phase contact line zone might be more complex.

Changes in Capillary Pressure. As the contact angle has been alternated under the dynamic flow process, it changes the pressure drop between the two points in the flow direction, crossing the curved CO_2–water interface. The total pressure drop in the flow region can be considered as $\Delta P = P_c + \Delta P_h$, where ΔP_h is the hydrodynamic pressure drop between the two points along the flow direction; and the capillary pressure P_c can be calculated from the Young–Laplace equation for the contact angles between the two infinite parallel plates

$$P_c = \frac{2\gamma \cos\theta_w}{h} \tag{3}$$

where h is the distance between the inner surfaces of the two plates, i.e., h = 6.57 nm here; θ_w is the water contact angle; and γ is the interfacial tension between water and CO_2. γ = 0.035 N/m is calculated from the CO_2–water interfacial simulations (see Section S6 in the Supporting Information for details). The value of P_c can vary at different flow velocities as the contact angle is a function of contact line velocity. We can plot P_c as a function of the contact line velocity v in Figure 5, by combining eqs 2 and 3, with $\lambda_{\parallel}$ = 0.456 nm, n = 4.8 nm^{-2}, and $K_{o,\parallel}$ = 21.7 GHz. It can be seen that P_c is highly dependent on v. The total pressure drop ΔP can be determined more accurately if the effect of the flow velocity on the contact angle is taken into consideration. To check the validity of the Young–Laplace equation at the nanoscale, the Young–Laplace equation is used to estimate the interfacial tension between

DOI: 10.1021/acs.langmuir.9b00076
Langmuir 2019, 35, 5324–5332

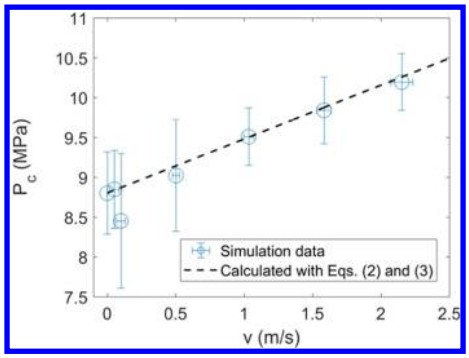

Figure 5. Capillary pressure calculated from the contact angles at different contact line velocities using the Young–Laplace equation. Dashed line is the analytical prediction calculated using eqs 2 and 3 with $\lambda_{\parallel}$ = 0.456 nm, n = 4.8 nm^{-2}, and $K_{o,\parallel}$ = 21.7 GHz.

CO_2 and water using the bulk pressure differences and the calculated contact angle, which is shown in Figure S4 in the Supporting Information. Values of interfacial tension calculated from the Young–Laplace equation were found to be greater than those calculated from the CO_2–water interfacial simulations, but both results seem to follow a similar trend. The differences may be due to the deviation of the pressure on the CO_2–silica and water–silica interfaces from the bulk pressure. Other possible factors such as the inaccurate definition of the channel height at the nanoscale and errors in measuring the contact angle at the nanoscale should also be considered. Hence, the Young–Laplace equation only gives an estimation of the capillary pressure P_c at different velocities at the nanoscale.

Comparison with Empirical Equations. There are empirical equations for the contact angle and capillary number relation obtained from the experiments. The empirical equations can be expressed using a universal form for $C_a < 10^{-2}$, as suggested by Seebergh and Berg[24]

$$H = \frac{\cos\theta_s - \cos\theta_d}{\cos\theta_s + 1} = AC_a{}^{B} \tag{4}$$

where A and B are the correlation parameters obtained by fitting the data. It should be noted that the parameters of the empirical equations obtained from experiments were derived with liquid as the advancing fluid, whereas in our analyses, supercritical CO_2 is the advancing fluid. Figure 6 compares our simulation results and the corresponding fitted line using eq 4

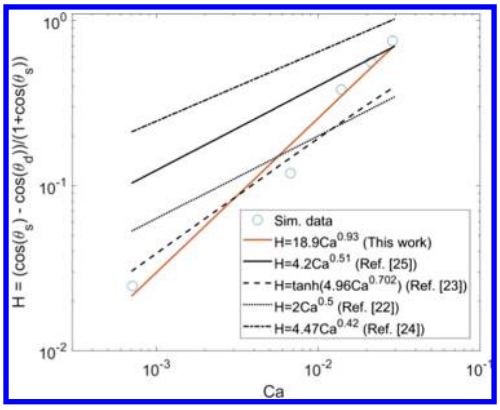

Figure 6. Comparison of the fitted equation (H = 18.9$C_a{}^{0.93}$) from this work with the other empirical equations from the literature.[22−25]

with results obtained from the literature. Here, the viscosity of water is assumed to be the same as the experimental data,[67] i.e., μ = 0.469 mPa s at 10.6 MPa and 333.15 K, to calculate C_a. It is noted that the data point obtained from our MD simulations with v_p = 0.1 m/s is not shown in Figure 6 and is not used for the fitting, because their average values of $\cos(\theta_s) - \cos(\theta_d)$ is negative and cannot be plotted in a log–log plot. Our fitted line has a B value close to 1, which indicates that $\cos(\theta_s) - \cos(\theta_d)$ varies linearly with v. The empirical functions of Li et al.[25] and Seebergh and Berg[24] result in larger H values than ours. However, our results are close to those from Jiang et al.[23] and Bracket et al.[22] (Figure 6). This may be due to the fact that the experiments of Li et al.[25] and Seebergh and Berg[24] have carried out in the low C_a region, whereas Jiang et al.[23] and Bracket et al.[22] fitted the data in a relatively high C_a region ($C_a > 10^{-3}$), which was also pointed out by Li et al.[25] This may be the reason why our results are closer to those of Jiang et al.[23] and Bracket et al.[22] than those of Li et al.[25] and Seebergh and Berg.[24] In addition, our system has a supercritical CO_2 phase instead of the air phase and is carried out at the nanoscale, and the fluids are confined within two parallel plates under high pressure and high-temperature environments. All these factors can possibly affect the results such that our fitted line deviates from the existing empirical functions.

SUMMARY AND CONCLUSIONS

As the CO_2/water flow in CO_2 sequestration is a dynamic process, both static and dynamic wettability can be important for the structural and residual trapping mechanisms. This study has demonstrated that MD simulations can predict the dependence of the nanoscale dynamic wetting on the contact line velocity for CO_2–water–silica surfaces, under reservoir conditions. The contact angles at different contact line velocities were calculated for the CO_2–water–silica system. Based on the MKT, the equilibrium jump frequencies ($K_{o,\perp}$ and $K_{o,\parallel}$) of the CO_2 and water molecules on the silica surface were estimated from the MD coordinate data, given the perpendicular and parallel jump distances ($\lambda_{\perp}$ and $\lambda_{\parallel}$). $\lambda_{\perp}$ was calculated from the CO_2 and water density profiles on the silica surface and $\lambda_{\parallel}$ was calculated from the area density of the silanol groups on the silica surface. The MKT was also validated by comparing the calculated equilibrium jump frequencies with the values obtained from the fitting of the MKT equation (eq 2) against the calculated contact angles at different velocities. The change in wettability can contribute to the capillary pressure between CO_2 and water, which becomes significant at small pore radius, as estimated using the Young–Laplace equation. The simulation result of the dynamic contact angle was expressed in the empirical equation form and was compared to the previous empirical equations drawn from the experiments,[22−25] along with brief discussions. The incorporation of this dependence into pore-scale dynamic flow models can enhance the accuracy of reservoir-scale modeling of CO_2 sequestration. Since the formation of the reservoir can contain a mix of minerals and perhaps other fluids, such as oil, the behavior of dynamic contact angles at different velocities for other fluids and mineral surfaces can also be studied using MD simulations to better understand the mechanism.

DOI: 10.1021/acs.langmuir.9b00076
Langmuir 2019, 35, 5324−5332

■ ASSOCIATED CONTENT

Supporting Information

The Supporting Information is available free of charge on the ACS Publications website at DOI: 10.1021/acs.langmuir.9b00076.

Snapshot of the Q^3 silica surface structure (Section S1), the force field equations, and parameters used in the molecular dynamic simulations (Section S2), the simulation of a water droplet on the silica substrate (Section S3), the calculations of the contact angle (Section S4), the calculations of the cumulative percentage curve (Section S5), and the calculation of the interfacial tension from CO_2−water interface simulation (Section S6) (PDF)

■ AUTHOR INFORMATION

Corresponding Author

*E-mail: luming.shen@sydney.edu.au. Tel: +61-2-93512126. Fax: +61-2-93513343.

ORCID

Luming Shen: 0000-0001-6243-4304

Yixiang Gan: 0000-0002-9621-0277

Notes

The authors declare no competing financial interest.

■ ACKNOWLEDGMENTS

This work was supported in part by the Australian Research Council through Discovery Projects (DP170102886). P.H. acknowledges the financial support from The University of Sydney Nano Institute Postgraduate Top-Up Scholarship. This research was undertaken with the assistance of resources and services from the National Computational Infrastructure (NCI), which is supported by the Australian Government, and the University of Sydney HPC service at the University of Sydney.

■ REFERENCES

(1) Yang, F.; Bai, B.; Tang, D.; Shari, D.-N.; David, W. Characteristics of CO 2 sequestration in saline aquifers. *Pet. Sci.* **2010**, *7*, 83−92.

(2) Jung, J.-W.; Wan, J. Supercritical CO2 and ionic strength effects on wettability of silica surfaces: Equilibrium contact angle measurements. *Energy Fuels* **2012**, *26*, 6053−6059.

(3) Sarmadivaleh, M.; Al-Yaseri, A. Z.; Iglauer, S. Influence of temperature and pressure on quartz−water−CO2 contact angle and CO2−water interfacial tension. *J. Colloid Interface Sci.* **2015**, *441*, 59−64.

(4) Espinoza, D. N.; Santamarina, J. C. Water-CO2-mineral systems: Interfacial tension, contact angle, and diffusion—Implications to CO2 geological storage. *Water Resour. Res.* **2010**, *46* (7), W07537.

(5) Iglauer, S.; Pentland, C.; Busch, A. CO2 wettability of seal and reservoir rocks and the implications for carbon geo-sequestration. *Water Resour. Res.* **2015**, *51*, 729−774.

(6) Chen, C.; Dong, B.; Zhang, N.; Li, W.; Song, Y. Pressure and temperature dependence of contact angles for CO2/water/silica systems predicted by molecular dynamics simulations. *Energy Fuels* **2016**, *30*, 5027−5034.

(7) Iglauer, S.; Mathew, M.; Bresme, F. Molecular dynamics computations of brine−CO2 interfacial tensions and brine−CO2−quartz contact angles and their effects on structural and residual trapping mechanisms in carbon geo-sequestration. *J. Colloid Interface Sci.* **2012**, *386*, 405−414.

(8) Javanbakht, G.; Sedghi, M.; Welch, W.; Goual, L. Molecular dynamics simulations of CO2/water/quartz interfacial properties: Impact of CO2 dissolution in water. *Langmuir* **2015**, *31*, 5812−5819.

(9) Chen, C.; Zhang, N.; Li, W.; Song, Y. Water contact angle dependence with hydroxyl functional groups on silica surfaces under CO2 sequestration conditions. *Environ. Sci. Technol.* **2015**, *49*, 14680−14687.

(10) Iglauer, S.; Salamah, A.; Sarmadivaleh, M.; Liu, K.; Phan, C. Contamination of silica surfaces: Impact on water−CO2−quartz and glass contact angle measurements. *Int. J. Greenhouse Gas Control* **2014**, *22*, 325−328.

(11) Tenney, C. M.; Cygan, R. T. Molecular simulation of carbon dioxide, brine, and clay mineral interactions and determination of contact angles. *Environ. Sci. Technol.* **2014**, *48*, 2035−2042.

(12) Jafari, M.; Jung, J. Direct measurement of static and dynamic contact angles using a random micromodel considering geological CO2 sequestration. *Sustainability* **2017**, *9*, 2352.

(13) Lv, P.; Liu, Y.; Wang, Z.; Liu, S.; Jiang, L.; Chen, J.; Song, Y. In situ local contact angle measurement in a CO2−brine−sand system using microfocused X-ray CT. *Langmuir* **2017**, *33*, 3358−3366.

(14) Hamraoui, A.; Thuresson, K.; Nylander, T.; Yaminsky, V. Can a dynamic contact angle be understood in terms of a friction coefficient? *J. Colloid Interface Sci.* **2000**, *226*, 199−204.

(15) Maggi, F. Multiphase capillary rise of multicomponent miscible liquids. *Colloids Surf., A* **2012**, *415*, 119−124.

(16) Maggi, F.; Alonso-Marroquin, F. Multiphase capillary flows. *Int. J. Multiphase Flow* **2012**, *42*, 62−73.

(17) Chauvet, F.; Geoffroy, S.; Hamoumi, A.; Prat, M.; Joseph, P. Roles of gas in capillary filling of nanoslits. *Soft Matter* **2012**, *8*, 10738−10749.

(18) Oyarzua, E.; Walther, J. H.; Mejia, A.; Zambrano, H. A. Early regimes of water capillary flow in slit silica nanochannels. *Phys. Chem. Chem. Phys.* **2015**, *17*, 14731−14739.

(19) Hultmark, M.; Aristoff, J. M.; Stone, H. A. The influence of the gas phase on liquid imbibition in capillary tubes. *J. Fluid Mech.* **2011**, *678*, 600−606.

(20) Stroberg, W.; Keten, S.; Liu, W. K. Hydrodynamics of capillary imbibition under nanoconfinement. *Langmuir* **2012**, *28*, 14488−14495.

(21) Martic, G.; Gentner, F.; Seveno, D.; Coulon, D.; De Coninck, J.; Blake, T. A molecular dynamics simulation of capillary imbibition. *Langmuir* **2002**, *18*, 7971−7976.

(22) Bracke, M.; De Voeght, F.; Joos, P. The kinetics of wetting: the dynamic contact angle. *Trends in Colloid and Interface Science III*; Springer, 1989; pp 142−149.

(23) Jiang, T.-S.; Soo-Gun, O.; Slattery, J. C. Correlation for dynamic contact angle. *J. Colloid Interface Sci.* **1979**, *69*, 74−77.

(24) Seebergh, J. E.; Berg, J. C. Dynamic wetting in the low capillary number regime. *Chem. Eng. Sci.* **1992**, *47*, 4455−4464.

(25) Li, X.; Fan, X.; Askounis, A.; Wu, K.; Sefiane, K.; Koutsos, V. An experimental study on dynamic pore wettability. *Chem. Eng. Sci.* **2013**, *104*, 988−997.

(26) Thompson, P. A.; Brinckerhoff, W.; Robbins, M. O. Microscopic studies of static and dynamic contact angles. *J. Adhes. Sci. Technol.* **1993**, *7*, 535−554.

(27) Koplik, J.; Banavar, J. R.; Willemsen, J. F. Molecular dynamics of fluid flow at solid surfaces. *Phys. Fluids A* **1989**, *1*, 781−794.

(28) Heine, D. R.; Grest, G. S.; Webb, E. B., III Spreading dynamics of polymer nanodroplets. *Phys. Rev. E* **2003**, *68*, No. 061603.

(29) Cox, R. The dynamics of the spreading of liquids on a solid surface. Part 1. Viscous flow. *J. Fluid Mech.* **1986**, *168*, 169−194.

(30) Blake, T.; Haynes, J. Kinetics of liquidliquid displacement. *J. Colloid Interface Sci.* **1969**, *30*, 421−423.

(31) De Ruijter, M. J.; Blake, T.; De Coninck, J. Dynamic wetting studied by molecular modeling simulations of droplet spreading. *Langmuir* **1999**, *15*, 7836−7847.

(32) Bertrand, E.; Blake, T. D.; De Coninck, J. Influence of solid−liquid interactions on dynamic wetting: a molecular dynamics study. *J. Phys.: Condens. Matter* **2009**, *21*, No. 464124.

DOI: 10.1021/acs.langmuir.9b00076
Langmuir 2019, 35, 5324−5332

(33) Saraji, S.; Goual, L.; Piri, M.; Plancher, H. Wettability of supercritical carbon dioxide/water/quartz systems: simultaneous measurement of contact angle and interfacial tension at reservoir conditions. *Langmuir* **2013**, *29*, 6856−6866.
(34) Farokhpoor, R.; Bjørkvik, B. J.; Lindeberg, E.; Torsæter, O. Wettability behaviour of CO2 at storage conditions. *Int. J. Greenhouse Gas Control* **2013**, *12*, 18−25.
(35) Blake, T.; Clarke, A.; De Coninck, J.; De Ruijter, M. J. Contact angle relaxation during droplet spreading: comparison between molecular kinetic theory and molecular dynamics. *Langmuir* **1997**, *13*, 2164−2166.
(36) Thompson, P. A.; Robbins, M. O. Simulations of contact-line motion: slip and the dynamic contact angle. *Phys. Rev. Lett.* **1989**, *63*, 766.
(37) Blake, T.; Bracke, M.; Shikhmurzaev, Y. Experimental evidence of nonlocal hydrodynamic influence on the dynamic contact angle. *Phys. Fluids* **1999**, *11*, 1995−2007.
(38) Xu, S.-H.; Wang, C.-X.; Sun, Z.-W.; Hu, W.-R. The influence of contact line velocity and acceleration on the dynamic contact angle: An experimental study in microgravity. *Int. J. Heat Mass Transfer* **2011**, *54*, 2222−2225.
(39) Nieto-Draghi, C.; de Bruin, T.; Pérez-Pellitero, J.; Bonet Avalos, J.; Mackie, A. D. Thermodynamic and transport properties of carbon dioxide from molecular simulation. *J. Chem. Phys.* **2007**, *126*, No. 064509.
(40) Vega, C.; De Miguel, E. Surface tension of the most popular models of water by using the test-area simulation method. *J. Chem. Phys.* **2007**, *126*, No. 154707.
(41) Emami, F. S.; Puddu, V.; Berry, R. J.; Varshney, V.; Patwardhan, S. V.; Perry, C. C.; Heinz, H. Force field and a surface model database for silica to simulate interfacial properties in atomic resolution. *Chem. Mater.* **2014**, *26*, 2647−2658.
(42) Zhuravlev, L. The surface chemistry of amorphous silica. Zhuravlev model. *Colloids Surf., A* **2000**, *173*, 1−38.
(43) Plimpton, S. Fast parallel algorithms for short-range molecular dynamics. *J. Comput. Phys.* **1995**, *117*, 1−19.
(44) Humphrey, W.; Dalke, A.; Schulten, K. VMD: visual molecular dynamics. *J. Mol. Graphics* **1996**, *14*, 33−38.
(45) Kohlmeyer, A. *TopoTools*, 2017. http://doi.org/10.5281/zenodo.545655.
(46) Weijs, J. H.; Marchand, A.; Andreotti, B.; Lohse, D.; Snoeijer, J. H. Origin of line tension for a Lennard-Jones nanodroplet. *Phys. Fluids* **2011**, *23*, No. 022001.
(47) Ryckaert, J.-P.; Ciccotti, G.; Berendsen, H. J. Numerical integration of the cartesian equations of motion of a system with constraints: molecular dynamics of n-alkanes. *J. Comput. Phys.* **1977**, *23*, 327−341.
(48) Hockney, R. W.; Eastwood, J. W. *Computer Simulation Using Particles*; CRC Press, 1988.
(49) Yeh, I.-C.; Berkowitz, M. L. Ewald summation for systems with slab geometry. *J. Chem. Phys.* **1999**, *111*, 3155−3162.
(50) Lamb, R. N.; Furlong, D. N. Controlled wettability of quartz surfaces. *J. Chem. Soc., Faraday Trans. 1* **1982**, *78*, 61−73.
(51) Schneider, T.; Stoll, E. Molecular-dynamics study of a three-dimensional one-component model for distortive phase transitions. *Phys. Rev. B* **1978**, *17*, 1302.
(52) Shinoda, W.; Shiga, M.; Mikami, M. Rapid estimation of elastic constants by molecular dynamics simulation under constant stress. *Phys. Rev. B* **2004**, *69*, No. 134103.
(53) Young, T., III. An essay on the cohesion of fluids. *Philos. Trans. R. Soc. London* **1805**, 65−87.
(54) Seveno, D.; Blake, T. D.; De Coninck, J. Young's equation at the nanoscale. *Phys. Rev. Lett.* **2013**, *111*, No. 096101.
(55) Fernandez-Toledano, J.; Blake, T.; De Coninck, J. Young's equation for a two-liquid system on the nanometer scale. *Langmuir* **2017**, *33*, 2929−2938.
(56) Das, S. K.; Binder, K. Does Young's equation hold on the nanoscale? A Monte Carlo test for the binary Lennard-Jones fluid. *Europhys. Lett.* **2010**, *92*, No. 26006.
(57) Dickson, J. L.; Gupta, G.; Horozov, T. S.; Binks, B. P.; Johnston, K. P. Wetting phenomena at the CO2/water/glass interface. *Langmuir* **2006**, *22*, 2161−2170.
(58) Li, X.; Fan, X. Effect of CO2 phase on contact angle in oil-wet and water-wet pores. *Int. J. Greenhouse Gas Control* **2015**, *36*, 106−113.
(59) Bikkina, P. K. Contact angle measurements of CO2−water−quartz/calcite systems in the perspective of carbon sequestration. *Int. J. Greenhouse Gas Control* **2011**, *5*, 1259−1271.
(60) Rohatgi, A. *WebPlotDigitizer*, version 4.1. https://automeris.io/WebPlotDigitizer, 2018.
(61) Blake, T. D.; De Coninck, J. The influence of solid−liquid interactions on dynamic wetting. *Adv. Colloid Interface Sci.* **2002**, *96*, 21−36.
(62) Glasstone, S.; Eyring, H.; Laidler, K. J. *The Theory of Rate Processes*; McGraw-Hill, 1941.
(63) Blake, T. D. The physics of moving wetting lines. *J. Colloid Interface Sci.* **2006**, *299*, 1−13.
(64) Ramiasa, M.; Ralston, J.; Fetzer, R.; Sedev, R. Contact line friction in liquid−liquid displacement on hydrophobic surfaces. *J. Phys. Chem. C* **2011**, *115*, 24975−24986.
(65) Ma, M. D.; Shen, L.; Sheridan, J.; Liu, J. Z.; Chen, C.; Zheng, Q. Friction of water slipping in carbon nanotubes. *Phys. Rev. E* **2011**, *83*, No. 036316.
(66) Allen, M. P.; Tildesley, D. J. *Computer Simulation of Liquids*; Oxford University Press: New York, 1987.
(67) Lemmon, E. W.; McLinden, M. O.; Friend, D. G. Thermophysical Properties of Fluid Systems. In *NIST Chemistry WebBook*; Linstrom, P. J., Mallard, W. G., Eds.; NIST Standard Reference Database Number 69; National Institute of Standards and Technology: Gaithersburg, MD, 2018; p 20899.

DOI: 10.1021/acs.langmuir.9b00076
Langmuir 2019, 35, 5324−5332